TEMPERATURE MEASUREMENTS OF THE NSLS-II VACUUM COMPONENTS*

A. Blednykh†, G. Bassi, C. Hetzel, B.N. Kosciuk,
D. Padrazo Jr, T.V. Shaftan, V.V. Smaluk, G.M. Wang
Brookhaven National Laboratory, Upton, NY, USA

Abstract

This paper is dedicated to the analysis of our recent experience from ramp-up of operating current at NSLS-II from 25 mA at the end of commissioning in 2014 to 475 mA achieved in studies today. To approach the design level of the ring intensity we had to solve major problems in overheating of the chamber components. Since the beginning of the NSLS-II commissioning, the temperature of the vacuum components has been monitored by the Resistance Temperature Detectors (RTDs) located predominantly outside of the vacuum chamber and attached to the chamber body. A several vacuum components were designed with the possibility for internal temperature measurements under the vacuum as diagnostic assemblies. Temperature map helps us to control overheating of the vacuum components around the ring especially during the current ramp-up. The average current of 475mA has been achieved with two main 500MHz RF cavities and w/o any harmonic cavities.

INTRODUCTION

The experimental data collected with $M = 1000$ number of bunches for the regular operational lattice with all IDs magnet gap closed at $V_{RF} = 3MV$. It corresponds to $\sigma_s(I_0 \to 0) = 4.4mm$ bunch length at low current. The RF voltage is induced by two superconducting 500MHz CESR-B RF cavities installed back-to-back in Cell 24. Up to 4 RF cavities are planned to be used for a maximum deliverable RF voltage $V_{RF} = 4.5MV$, corresponding to $\sigma_s(I_0 \to 0) = 3.6mm$. With all IDs installed, a voltage of $4.5MV$ will guarantee a momentum acceptance larger than 3%. The rms bunch length is short compared to the standard half-aperture of the vacuum chamber, i.e. $\sigma_s \ll b$.

BELLOWS

The internal RF contact fingers of the NSLS-II bellows are designed to follow the octagonal profile of the standard vacuum chamber and to minimize impedance contribution due to the outer bellows convolution. The 3D rendered picture of the NSLS-II bellows is shown in Fig. 1. The simplified internal connection of the RF contact fingers relative to the vacuum chamber is shown in Fig. 2, where $b = 12.5mm$ is the chamber radius, $L = 42mm$ is the length of the cavity type joint and $\Delta = 0.4mm$ is the sleeve thickness. The RF contact fingers are able to slide longitudinally with a good contact on the top of the octagonal sleeve under the RF spring force. Three individual bellows in NSLS-II were designed for internal temperature measurements by the Resistance Temperature Detectors (RTDs). A couple of RTDs were fixed on the top of the GLIDCOP RF contact fingers as it is shown in Fig. 3a. The experimental internal

temperature measurements are shown in Fig. 3b. The measured temperature (blue dots) has a quadratic dependence on the average current, $T \sim I_{av}^2$, where the dark cyan trace is the experimental data fit. The RF contact fingers heats up to $T = 65°C$ at $I_{av} = 400mA$ with $\sigma_s(I_0 \to 0) = 4.4mm$.
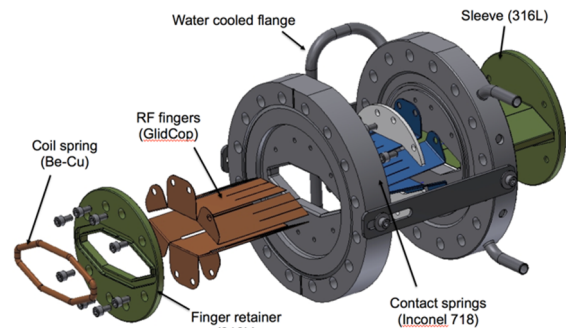

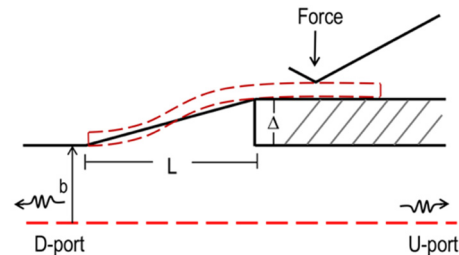Figure 1: 3D rendered picture of the bellows geometry.

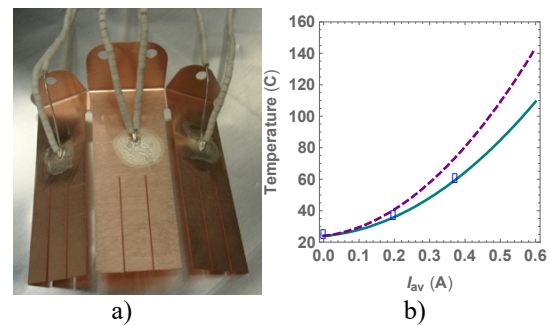Figure 2: Simplified 2D model of the bellows.

Figure 3: a) GLIDCOP RF fingers of the bellows with attached RTDs for internal temperature measurements. b) Internal temperature measurements at $V_{RF} = 3MV$ (blue dots) and the data fit (dark cyan solid line). The dashed purple line is the predicted data at $V_{RF} = 4.5MV$.

To estimate the temperature rise for a shorter bunch length, the numerical simulations of the bellows geometry with a perfect contact of the RF contact fingers have been performed by the GdfidL code [1]. The real part of the longitudinal impedance $\mathrm{Re}Z_{\parallel}$ is shown in Fig. 4. Several

trapped modes are generated due to the cavity shape configuration of the geometry within the bunch spectrum of the beam. Those modes contribute to the geometric loss factor k_{loss}^{geom} (Fig. 5) The total loss factor is plotted as a sum of k_{loss}^{geom} and resistive wall loss factor k_{loss}^{rw} and it is inversely proportional to the bunch length within the considered range of σ_s (Fig. 5, purple trace). Based on these simulations, we estimated the temperature rise for a $\sigma_s(I_0 \to 0) = 3.6mm$ bunch length in Fig. 3b (purple dashed trace).
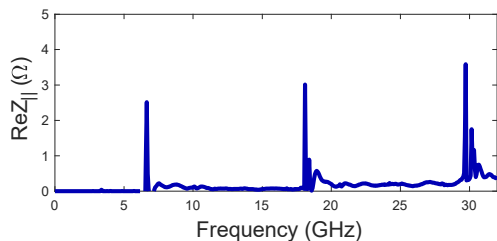

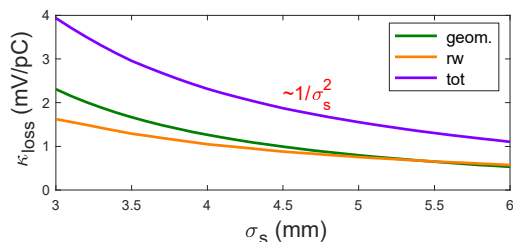Figure 4: The real part of the longitudinal impedance.

Figure 5: The loss factor as a function of bunch length for the bellows geometry.

STRIPLINE

To correlate the numerical simulations of the beam impedance and the heat transfer analysis with the experimental data, a special diagnostic stripline with two $\phi = 60°$ angle electrodes and 6 infrared (IR) view ports of 16mm diameter has been designed for internal temperature measurements (Fig. 6). The copper coated chamber was outfitted with six view ports, three per stripline so that the infrared detector can view the stripline in the center and at the ends. Two electrodes are located inside of the round pipe with a $d = 39.6mm$ radius. The length of electrodes is $L = 160mm$ with a $2mm$ thickness. The electrodes are elevated relative to the vacuum chamber center by $\Delta = 2mm$ from a $b = 25.2mm$ radius.
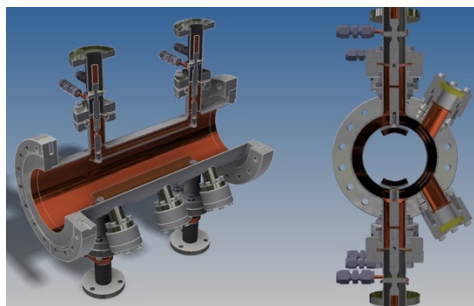

Figure 6: Diagnostic stripline with six IR view ports.

The experimental internal temperature data for the stripline geometry measured by the IR spot detector through the IR view port is shown in Fig. 7 (red dots). As can be seen from the experimental data fit (red trace), each individual electrode will heat up to a $T \approx 100°C$ temperature at $I_{av} = 500mA$ with a $\sigma_s(I_0 \to 0) = 3.6mm$ bunch length.
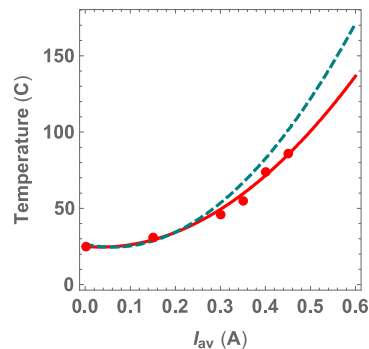

Figure 7: The internal temperature of the stripline electrodes vs. average current measured by the IR temperature detector (red dots). The red solid line is the data fit at $V_{RF} = 3MV$. The dashed dark cyan line is the predicted data at $V_{RF} = 4.5MV$.

To scale the experimental temperature data for shorter bunch length, $ReZ_{||}$ and k_{loss} have been simulating and the results are presented in Fig. 8 and Fig. 9. The loss factor is inversely proportional to the bunch length within the considered range of the bunch length. As can be seen from Fig. 8, $ReZ_{||}$ does not change significantly at high frequency, where the bunch spectrum will be increased in frequency from $22GHz$ ($\sigma_s = 4.4mm$) to $27GHz$ ($\sigma_s = 3.6mm$).
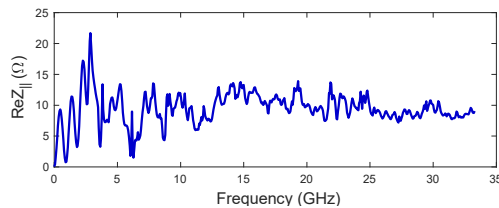

Figure 8: The real part of the longitudinal impedance for the diagnostic stripline.
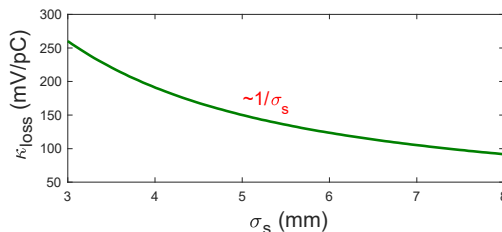

Figure 9: The geometric loss factor as a function bunch length for the diagnostic stripline. The resistive wall contribution is small enough and it is omitted on this plot.

The coupling impedance (Fig. 8) for the stripline geometry can be considered as a sum of the low and high frequency impedances. The longitudinal impedance at low frequency, $f < f_{c,E01}$, can be approximated by [2]

$$\mathrm{Re}Z_{||}(k) = g_{||}^2 Z_{chsl,||}\sin^2(kL) \qquad (1)$$

where $k = 2\pi f/c$ is the wave number, $f_{c,E01}$ is the cut-off frequency of the vacuum chamber for the fundamental E_{01}-mode, L is the longitudinal length of the electrodes, $g_{||}$ is the longitudinal geometric factor and $Z_{chsl,||}$ is the characteristic impedance of the stripline.

The values of $g_{||}$ and $Z_{ch,||}$ in Eq. (1) can be found analytically or numerically by solving Laplace's equation in 2 dimensions. The longitudinal geometric factor $g_{||}$ for the simplified circular geometry (Fig. 10a) is given by [3]

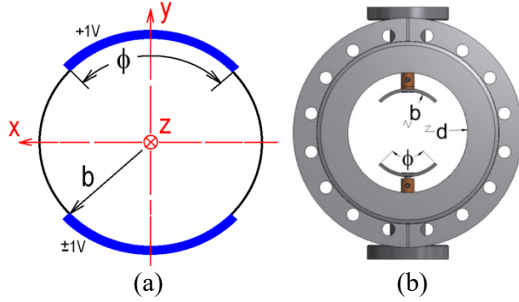$$g_{||} = \phi/\pi. \qquad (2)$$

Figure 10: Stripline geometry. a) Simplified model. b) Kicker geometry installed in NSLS-II.

However, $g_{||}(\phi)$ for the simplified geometry differs from the numerically simulated $g_{||}(\phi)$ for the real stripline kicker geometry (Fig. 10b). The results of the comparison are presented in Fig. 11.
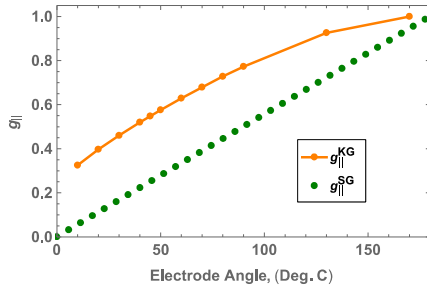

Figure 11: Longitudinal geometric factor as a function of electrode angle ϕ for simplified geometry (SG) and for the stripline kicker geometry (KG).

The longitudinal characteristic impedance $Z_{chsl,||}$ for the stripline geometry can be approximated by

$$Z_{chsl,||} = Z_{cxl}/\sqrt{g_{||}}, \quad Z_{cxl} = \frac{Z_0}{2\pi}\log(d/b), \qquad (3)$$

where Z_{cxl} is the characteristic impedance of the coaxial (CXL) transmission line and $g_{||}$ is the longitudinal geometric factor of Eq. (2). The results of the comparison for $Z_{chsl,||}$ between the 2D POISSON code and Eq. (3) are shown in Fig. 12 for different values of the electrode angle ϕ.
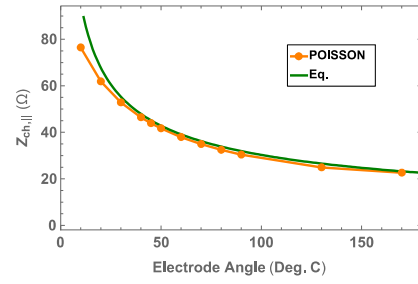

Figure 12: The longitudinal (orange) and transverse (green) characteristic impedances as a function of electrode angle ϕ calculated using the POISSON code for the stripline kicker geometry.

For the stripline geometry we can identify the "step regime", where the longitudinal impedance $\mathrm{Re}Z_{sl,||}$ is frequency independent at frequencies much higher than $f_{c,E01}$, and can be approximated by

$$\mathrm{Re}Z_{sl,||} = \frac{Z_{cxl}}{2} = \frac{Z_0}{4\pi}\log\left(\frac{d}{b}\right), \qquad (4)$$

where Z_{cxl} is given in Eq. (3). It should be noted here, that Eq. (4) for the stripline geometry in the step regime is four times smaller than Heifets formula [4] for the step transition geometry. To distinguish the contribution of the impedance to the loss factor below and above $f_{c,E01}$, we define

$$k_L(k_1,k_2) = \frac{c}{\pi}\int_{k_1}^{k_2}\mathrm{Re}Z_{||}(k)e^{-\sigma_s^2 k^2}\,dk, \qquad (5)$$

and split the loss factor in two parts, i.e. $k_{loss} = k_L(0,\infty) = k_{loss1} + k_{loss2}$, where $k_{loss1} = k_L(0,k_c)$, $k_{loss2} = k_L(k_c,\infty)$, and $k_c = 2\pi f_{c,E01}/c$. Using Eq. (1) for k_{loss1} it follows, for $\sigma_s \ll L$, that

$$k_{loss1} = g_{||}^2 Z_{chsl,||}\frac{c}{4\sqrt{\pi}\sigma_s}\mathrm{erf}(\sigma_s k_c), \qquad (6)$$

where $\mathrm{erf}(x)$ is the error function. Analogously for k_{loss2}, using Eq. (4) it follows that

$$k_{loss2} = \frac{Z_{cxl}\,c}{4\sqrt{\pi}\sigma_s}\left(1 - \mathrm{erf}(\sigma_s k_c)\right). \qquad (7)$$

Eq. (6) and Eq. (7) are useful relations to investigate the loss factor behaviour below and above the cut-off frequency $f_{c,E01}$ as a function of bunch length σ_s.

REFERENCES

[1] W. Bruns, The GDFIDL Electromagnetic Field simulator, http://www.gdfidl.de/.

[2] R. Shafer, "Characteristics of Directional Coupler Beam Position Monitors," *IEEE Trans. Nucl. Sci.*, vol. NS-32, no. 5, pp. 1933-1937, Oct. 1985.

[3] K.-Y. Ng, "Impedances of Stripline Beam-Position Monitors," *Particle Accelerators*, vol. 23, pp. 93-102, Oct. 1987.

[4] B. W. Zotter and S. A. Kheifets, *Impedances and Wakes in High-Energy Particle Accelerators*. London, UK: World Scientific, 1998. doi:10.1142/3068